# Chapter 2

# SURFACE FORCING AND THE PLANETARY BOUNDARY LAYER

## 1 Surface Forcing

As noted in Chap. 1, almost all the forcing for the oceanic circulation occurs through the top surface. It is caused by the surface wind stress (sometimes transmitted through sea ice) and heat and water fluxes (Fig. 1). These forcing fields are familiar subjects in the study atmospheric circulation; so they will be described rather briefly.

The time-mean, near-surface wind pattern, $\mathbf{U}_a$, shows the expected features (Figs. 2-3): zonally-oriented tropical trade winds, mid-latitude westerlies, and weak polar easterlies; the Afro-Asian monsoon; and the standing-eddy circulations of sub-tropical anti-cyclones and sub-polar cyclones. In Chap. 1 we discussed many different types of currents that arise from the associated surface stress.

The mean meridional heat balance for the planet (Fig. 4) shows how the ocean contributes a substantial fraction of the meridional heat flux needed for climate equilibrium in order to balance the different meridional distributions of solar and infrared radiation for the Earth. The oceanic flux is especially important in the tropics and subtropics, and it is carried primarily by the meridional overturning circulation, both Ekman and thermohaline. Detailed maps of the distribution of surface heat flux are in Figs. 5-8. The geographical pattern of air-sea fluxes shows tropical and sub-tropical heating of the ocean and middle- and high-latitude cooling. The largest sustained air-sea fluxes occur near the largest currents, because they are capable of large lateral advective transports of heat that can resupply these sites of large vertical flux; note in particular the regions around the Gulf Stream, the Antarctic Circumpolar Current, the Agulhas Current, and the Equatorial Currents. The mean flux fields for fresh water are shown in Figs. 9-10. Note that water is delivered to the oceans in the subpolar regions, near most coastlines, and in the tropical rain zones, while it is removed from the ocean broadly in the subtropical zones. The mean summer and winter SST patterns are shown in Fig. 6. They show broad tropical pools with small SST gradients and broad patterns of decreasing temperature towards the poles. In particular, note how sharp the SST gradients are across the subtopical/subpolar fronts in the western North Atlantic and Pacific and across the Agulhas Retroflection south of Africa. These are, of course, advectively sharpened fronts.

The strong variability of the atmosphere on both synoptic (storm), seasonal, and interannual time scales causes surface fluxes on the same scales. So the ocean also has vigorous variability on these scales; typically, though, this directly forced variability weakens with increasing depth into the ocean interior for the material fields (*i.e.,* $T$ and $S$), and this depth-weakening is more rapid the higher the forcing frequency. The ocean does respond fairly efficiently to high-frequency

forcing in the barotropic velocity field, however; this occurs mainly in the form of barotropic (*a.k.a.* shallow-water) gravity, Kelvin (coastal), and Rossby waves, although there is also a substantial Sverdrup gyre and WBC barotropic circulation on seasonal forcing time scales. On longer forcing time scales of multiple years, the gyre and WBC currents evolve into a more baroclinic structure, concentrated in and above the main pycnocline.

# 2 Ekman Transport and Pumping

In Sec. 7 of Chap. 1, the dynamical relations were presented for Ekman transport, $\mathbf{T}^t_{ek}$, and pumping, $w^t$, for the surface boundary layer, along with the associated Sverdrup transport streamfunction, $\Psi$. All of these quantities are directly calculable from the surface wind stress, $\rho_o \boldsymbol{\tau}$, which in turn is calculated from the near-surface wind (Fig. 2) by an empirical regression formula,

$$\rho_o \boldsymbol{\tau} \;=\; \rho_a C_D |\mathbf{U}_a| \mathbf{U}_a \,, \tag{1}$$

where $\rho_a$ is a mean atmospheric density and $C_D \sim 10^{-3}$ is a drag coefficient (which varies both with near-surface atmospheric stratification and surface gravity waves).

Figure 11 shows the annual-mean Ekman transport, based on the same winds as in Fig. 2. It is noticeably turned away from the surface wind directions, to the right in the Northern Hemisphere and *vice versa* in the Southern Hemisphere. Figure 12 shows the surface Ekman pumping, which is the divergence of the Ekman transport, although this figure is based on a different wind climatology. It is mainly directed downward in subtropical gyres and upward in subpolar gyres.

Figure 12 also shows the associated Sverdrup transport pattern in the Atlantic. Note in particular the subpolar, subtropical, and even weak tropical gyres. The latter are the cause of the North Equatorial Countercurrent near $8^o$ N. Here $\Psi$ is depicted without including the mass-conserving recirculations near the western boundary. Lateral boundary-layer dynamics go beyond the relations presented in Chap. 1, and theories of several different types have been devised to account for the western boundary currents of the gyres (Robinson, 1963). The simplest of such theories invoke eddy viscosity — it acts both through the bottom Ekman boundary layer and/or through the lateral boundary layer, especially in the west — in place of the more realistic dynamics of mean-advection and mesoscale-eddy rectification. Solutions for these two models were first presented by Stommel (1948) and Munk (1950), respectively. This subject is addressed in Chap. 3.

Ekman and Sverdrup relations are widely believed to be accurate for much of the ocean away from strong currents. It is not easy to test them accurately with velocity observations because of sampling limitations. However, one fairly convincing confirmation is shown in Fig. 13, albeit in a location where no other competing dynamical influences are very strong.

# 3 Surface Gravity Wave Effects

While no oceanographer who ever took a research cruise in high winds has ever overlooked effects of surface gravity waves on ships, their effects on circulation have largely been ignored. In this section, I present, at some length, some theoretical arguments and empirical analyses that suggest this traditional view is not wholly correct.

## 3.1 Surface Waves and Stokes Drift

Rectification can also arise without any circulation instability. Consider the example of *Stokes drift* associated with surface gravity waves. Given a weak amplitude, inviscid, irrotational surface gravity wave with sea surface elevation anomaly,

$$\eta^w(x,y,t) \;=\; a\cos[kx-\sigma t]\,, \tag{2}$$

propagating to the east and with a deep-water dispersion relation, $\sigma \;=\; \sqrt{gk}$, then the Eulerian time mean current is zero,

$$\overline{\mathbf{u}(\mathbf{x},t)}^{E} \;=\; 0\,, \tag{3}$$

but the Lagrangian mean (the Stokes drift) is nonzero:

$$\mathbf{u}_{st}(z) \;\equiv\; \overline{\mathbf{u}(\mathbf{x},t)}^{L} \;=\; \overline{\int^t \mathbf{u}^w(\mathbf{x},s)\,ds\cdot\boldsymbol{\nabla}\mathbf{u}^w(\mathbf{x},t)} \;=\; \frac{1}{2}\sigma k a^2 e^{2kz}\hat{\mathbf{x}}, \quad z\le 0\,. \tag{4}$$

Here the average is taken following a fluid parcel $\mathbf{x}(\xi,t)$, with

$$\frac{d\mathbf{x}}{dt} \;=\; \mathbf{u}^w(\mathbf{x}),\;\; \mathbf{x}(\xi,0) \;=\; \xi\,. \tag{5}$$

See Fig. 14 for a kinematic illustration of how Stokes drift arises because of surface intensification of the wave velocity, so that a parcel moves farther to the east when it is nearer the surface than it moves to the west when it is farther from the surface. The Stokes drift is confined to near the ocean surface on a scale $k^{-1} \sim 10$ m for a typical dominant gravity wave with wavelength $\lambda \;=\; 2\pi/k \;=\; 60$ m. Real oceanic waves exhibit a broad-band spectrum in $\mathbf{k}$, so the real Stokes drift is a superposition of contributions from many different wavenumbers.

## 3.2 Wave-Averaged Dynamics

The Stokes drift is a wave-driven Lagrangian circulation. As such we can expect it to transport any material property,

$$\frac{\partial\overline{c}}{\partial t} \;=\; \ldots\; -\,\mathbf{u}_{st}\cdot\boldsymbol{\nabla}\overline{c}\,, \tag{6}$$

and it contributes to the mean dynamics as an added advection, which is quite different from an eddy diffusion. There is also a Stokes-drift contribution to the mean horizontal momentum balance, through what is called the *vortex force*,

$$\frac{\partial \overline{\mathbf{u}}}{\partial t} \;=\; ... \;+ \mathbf{u}_{st} \times \left( f\hat{\mathbf{z}} + \overline{\boldsymbol{\zeta}} \right) \;. \tag{7}$$

The vortex force plays an essential role in the theory of Langmuir circulations (*i.e.,* wind- and wave-aligned overturning cells within the surface PBL, often seen because they trap buoyant debris along lines of surface convergence; Craik and Leibovich (1976) and McWilliams et al. (1997)).

The wave-averaged, free-surface, kinematic and constant-pressure boundary conditions also have wave-averaged terms which are important on a horizontal scale of wave modulation:

$$w \;=\; \boldsymbol{\nabla} \cdot \mathbf{M} \quad \phi - g\eta - p_a/\rho_o \;=\; -P \,, \tag{8}$$

at mean sea level, $z = 0$. Here $p_a$ is the atmospheric surface pressure and

$$\begin{aligned} \mathbf{M} &= \int_{-\infty}^{0} \mathbf{u}_{st} \, dz \\ P &= \overline{(\eta_t^w)^2} \,. \end{aligned} \tag{9}$$

The wave-averaged stress and buoyancy flux conditions do not contribute any significant wave-added terms for the circulation dynamics. The conditions (8) generalize the usual rigid-lid and surface pressure conditions when wave-effects are neglected. Notice in the pressure condition in (8) the possibilities of an *inverse barometer* response (where $\eta \;\approx\; -gp_a/rho_o$) and the diagnostic relation between dynamic pressure and sea level (where $\phi(z \;\approx\; 0) \;\approx\; g\eta$) that is the basis for altimetric estimations of surface geostrophic current. In both relations, the wave-added term, $P$, may provide an important modification; it turns out that the effect of $P$ is expressed felt in $\phi(0)$ rather than $\eta$ in deep water, but the $\eta$ expression can be strong near coastlines (where it is referred to as *wave set up*). I skip the derivations of (6)-(9), which are lengthy and subtle (McWilliams and Restrepo, 1999; McWilliams et al., 2004).

Now we consider how the additional wave-averaged terms lead to a generalization of the Ekman-Sverdrup theory for large-scale, mid-latitude gyres, including some empirical estimates of the size and geographical distribution of the wave-averaged contributions. The nonlinear vortex force in (7) can be neglected by the classical assumption of small Rossby number for the general circulation dynamics in the interior of a wind-gyre, but the Coriolis vortex force is important in the Ekman layer balance:

$$f\hat{\mathbf{z}} \times \mathbf{u}_{ek} \;=\; -\frac{\partial}{\partial z} \overline{\mathbf{u}_h' w'} - f\hat{\mathbf{z}} \times \mathbf{u}_{st} \,; \tag{10}$$

here the explicitly appearing average is understood to be over the PBL turbulent motions. The surface boundary condition is that the Reynolds stress equals the wind stress, $\rho_o \boldsymbol{\tau}$, and the interior boundary condition is that $\mathbf{u}_{ek}$ and the Reynolds stress vanish as $z \to -\infty$. The vertical profile

of Ekman current, $\mathbf{u}_{ek}(z)$, depends upon the profile of the Reynolds stress; however, the vertically integrated Ekman transport does not. The vertical integral of (10) is

$$\mathbf{T}_{ek} \;=\; -\hat{\mathbf{z}} \times \frac{\boldsymbol{\tau}}{\rho_o f} - \mathbf{T}_{st}\,, \tag{11}$$

where the boundary layer transports are defined by

$$\mathbf{T}_{ek} \;\equiv\; \int_{-\infty}^{0} \mathbf{u}_{ek}\, dz, \quad \mathbf{T}_{st} \;\equiv\; \int_{-\infty}^{0} \mathbf{u}_{st}\, dz\,. \tag{12}$$

Stokes drift decays away from the surface on a vertical scale $|\mathbf{k}|^{-1} \;\sim\; 10$ m, which is usually somewhat smaller than the PBL depth. Thus, the Eulerian Ekman transport has an "up-wave" contribution that cancels the Lagrangian transport of the Stokes drift, as well as a component perpendicular to the wind stress; *i.e.,* it is the total Lagrangian transport in the boundary layer (*i.e.,* the sum of the Eulerian-mean and Stokes drift transport from the waves) that is perpendicular to the wind stress.

Next consider Ekman pumping. We integrate the continuity equation over the boundary layer, using the wave-modified boundary condition (8) for $w$ at $z = 0$. The result is

$$\begin{aligned} w^t &= \boldsymbol{\nabla}_h \cdot \mathbf{T}_{ek} + \boldsymbol{\nabla}_h \cdot \mathbf{M} \\ &= \mathrm{curl}\left[\frac{\boldsymbol{\tau}}{\rho_o f}\right] + \boldsymbol{\nabla}_h \cdot (\mathbf{M} - \mathbf{T}_{st}) \\ &= \mathrm{curl}\left[\frac{\boldsymbol{\tau}}{\rho_o f}\right], \end{aligned} \tag{13}$$

where $w^t$ is the Ekman pumping velocity at the base of the surface Ekman layer. We have used the definition for $\mathbf{M}$ in (9) to cancel the wave-induced effect in the Ekman pumping. This is because the Stokes drift divergence lowers the sea surface in (8) at exactly the rate that wave-induced effect in the Ekman layer divergence lifts the base of the Ekman layer. Ekman pumping provides a significant forcing for the geostrophic flow in the interior, so $\mathbf{u}_g$ also lacks a direct wave-driven effect.

We calculate the wave-modified Sverdrup transport by vertically integrating the horizontal momentum equations, assuming Ekman dynamics in the surface PBL, planetary vorticity balance in the interior, and negligible contributions from near the ocean bottom. The result for the meridional component of the total transport, $\mathbf{T}$, is

$$\begin{aligned} \beta T^{(y)} &= -\beta T_{st}^{(y)} + \frac{1}{\rho_o}\,\mathrm{curl}\,[\boldsymbol{\tau}] + f\boldsymbol{\nabla}_h \cdot [\mathbf{M} - \mathbf{T}_{st}] \\ &= -\beta T_{st}^{(y)} + \frac{1}{\rho_o}\,\mathrm{curl}\,[\boldsymbol{\tau}]\,, \end{aligned} \tag{14}$$

using the same cancellation as in the Ekman pumping relation. In addition, we can integrate the continuity equation over the whole depth to obtain

$$\boldsymbol{\nabla}_h \cdot \mathbf{T} \;=\; -\boldsymbol{\nabla}_h \cdot \mathbf{M} \;=\; -\boldsymbol{\nabla}_h \cdot \mathbf{T}_{st}\,. \tag{15}$$

This comprises a closed set of equations for the horizontal transport $\mathbf{T}$, given $\boldsymbol{\tau}$ and $\mathbf{T}_{st}$, which is a boundary-value problem in two spatial dimensions. It is easily solved in terms of a Lagrangian transport streamfunction $\Psi(x, y)$ defined by

$$\mathbf{T} + \mathbf{T}_{st} \equiv \hat{\mathbf{z}} \times \boldsymbol{\nabla}_h \Psi \,. \tag{16}$$

From (12) the differential equation for $\Psi$ is

$$\beta \Psi_x = \frac{1}{\rho_o} \,\mathrm{curl}\, [\boldsymbol{\tau}] \,. \tag{17}$$

This is easily integrated in $s$ with an eastern-boundary condition of no normal transport,

$$\Psi = 0 \;\text{ at } x = X_{east}(y) \,. \tag{18}$$

Notice that (17)-(18) have the form of the usual Sverdrup transport relations, except that here they refer to the Lagrangian rather than Eulerian transport streamfunction; to obtain the latter, the Stokes transport must be subtracted from $\mathrm{curl}\,[\boldsymbol{\tau}]$.

We see that there are potentially important wave-averaged effects on the surface Ekman currents, the Sverdrup transport, and the diagnostic calculation of $\phi(x.y, 0, t)$ from $\eta$ and $p_a$. An assessment of their magnitudes could be made by evaluating the relevant quantities from a wave climatology. However, since surface wind climatologies are both more complete and more readily available, we instead base our empirical estimates on a wind climatology from a re-analysis using an operational weather forecast model for the years 1979-1995 (Kalnay *et al.*, 1996). This also gives us estimates of the wind stress. In the estimates that follow we assume that the waves are fully developed and in local equilibrium with the local wind on circulation time scales, using empirical regression relations estimated by Pierson and Moskowitz (1964) and linear, conservative wave dynamics to relate the fitted wave spectrum to the quantities of interest here (*e.g.,* $\mathbf{T}_{st}$, $P$, *etc.*). Obviously, this is not entirely correct. In particular, these estimates do not include remotely generated swell waves that are often a substantial component of the wave field. Nevertheless, this initial assessment illustrates the nature of the wave effects on the circulation. It may later be possible to obtain improved estimates from a wave-dynamical model used in an operational forecasting mode, such as the one currently in use at the ECMWF.

Using the empirical relations for the Stokes transport and wind stress, we can derive an estimate for the ratio, $\mathcal{R}$, of the wave- and wind-driven components in (11) to expose its dependencies on the most geographically variable quantities (viz., $f$ and the surface wind, $\mathbf{U}_a$), ignoring its other dependencies. The result is

$$\mathcal{R} \propto |f \mathbf{U}_a| \,. \tag{19}$$

Thus, we see that a high wind regime favors the wave-driving influence, while weak winds favor the wind-driving unless the local waves are enhanced through remotely generated swell. Moreover, the wave-driving influence tends to increase with latitude since $|f|$ does, and we can attribute this to the decrease in the Ekman-layer depth. Since wind speeds also tend to be larger in middle and higher latitudes, at least in winter, both factors in (19) indicate that wave-driving is relatively more important in these regions.

### 3.3 Stokes Transport and Sea-Level Bias

Now consider climatological estimates of various quantities above:

Fig. 15: The mean strength of the waves, $\overline{(\eta^w)^2}$, shows they are strongest in the midst of the westerly winds, away from land, and the variance ranges from less than 0.5 $m^2$ in the tropics to more than 3 $m^2$ in both hemispheres.

Fig. 16: The Stokes transport, $\mathbf{T}_{st}$, has the strongest values in the westerly wind regime between about $40^o$ and $60^o$, with a magnitude approaching 1 $m^2\ s^{-1}$. The magnitude of the Ekman transport (*cf.,* Fig. 6) is much larger than the Stokes transport near the equator, but these quantities have opposite trends with increasing latitude.

Fig. 17: The Stokes transport fraction, $\mathcal{R}$, is very small in the tropics, but it grows to a level of more than 40% of the Lagrangian Ekman transport at higher latitudes.

Previous empirical tests of Ekman and Sverdrup transport relations have largely been confined to relatively low latitudes. From Fig. 13, it is clear that this is a region where they are best satisfied and the wave effects are smallest. The present status of the theory presented here is that its predictions need observational or laboratory testing. An OGCM could easily be generalized to incorporate the wave-added dynamical effects derived here, given a suitable data set for the wave field (like those for the surface forcing).

## 4 Planetary Boundary Layer

The Planetary Boundary Layer (PBL) near the surface is a layer of thickness $\mathcal{O}(10-100)$ m, within which there is vigorous turbulence because of the fluid instabilities induced by surface fluxes. There is also rapid time variability of the turbulence-averaged profiles because of flux variability on the atmospheric meso- and synoptic-scales.

The turbulence itself is an important subject of scientific research, but we will not pursue it in this course. Suffice it say here that a parameterization model for PBL turbulent transports is required to diagnose and interpret the distributions near the surface, as well as a necessary element of an OGCM ((Chap. 7) (Large et al., 1994; Large, 1998).

Illustrative profiles of $T(z)$, $S(z)$, and $\mathbf{u}_h(z)$ are shown in Fig. 18. The material properties are fairly well mixed near the surface but have strong, and sometimes multiple, intervals of high gradient beneath the mixed layer, reflecting the time history of penetrative mixing and restratification. This figure shows before and after a fairly strong storm early in the fall.

A typical diurnal cycle is illustrated in Fig. 19. During the solar-heated part of the day, a near-surface stratified layer builds up (*n.b.,* 0.2 K over 20 m depth). During the dark part of the day, the

boundary layer deepens and this diurnal stratification is destroyed by vertical mixing. The kinetic energy dissipation rate $\epsilon$ is highly variable, but it is significantly larger within the PBL than below, even as the boundary layer depth varies.

A typical extratropical seasonal cycle in the mixed-layer $T(z)$ is shown in Fig. 20. The layer is shallow in summer due to stabilizing insolation and relatively weak wind-induced mixing by shear instability. The maximum surface temperature occurs in the late summer or early fall, lagging behind the peak insolation of early summer. During the fall through a sequence of storms, the layer deepens until it reaches its maximum in late winter. During the spring there is a sequence of restratification events caused by the increasing isolation, punctuated by re-deepening events from storms, and gradually the restratification dominates over the storminess as the season progresses toward Summer.

# 5 Downward Influences

One of the most subtle issues in oceanography is the dynamical and material communication between the surface layer and the interior. The surface layer is in direct contact with the atmosphere, and its fields — *e.g.,* Ekman current (Fig. 11), SST (Fig. 6), surface salinity (not shown, but characterized by relatively fresh water in the sub-polar, polar, and equatorial zones and by relatively salty water in the sub-tropical zones), and even surface waves (Fig. 15) — strongly reflect this air-sea interaction. In contrast, the oceanic interior is somewhat insulated from direct atmospheric influences, especially ones that vary rapidly (*i.e.,* on synoptic scales or even faster).

For large-scale currents the most effective communication is through the vortex stretching due to Ekman pumping and implicit in the Sverdrup transport relations (Chap. 1, Sec. 6). These establish interior horizontal pressure gradients and associated geostrophic currents, and they also advect materials vertically. Particular attention should be given to locations where interior iso(potential)pycnal surfaces intersect the surface, or equivalently, the surface planetary boundary layer; this is referred to as *outcropping*. When the flow is upward into the PBL ($w^t > 0$), interior water masses are exposed to the local air-sea fluxes and their material concentrations are effectively mixed with the flux-altered water by the PBL turbulence; this is referred to as *water mass transformation* in association with *upwelling*. When the flow is downward ($w^t < 0$), the altered water masses are carried down into the interior (*subduction*). While in the interior the material concentrations change relatively slowly compared to the rapid transformations in the PBL; thus, they can be considered as quasi-adiabatic, with stirring along isopycnals by mesoscale eddies (*cf.,* Chap. 1, Sec. 7) occurring much more efficiently than mixing across isocpycnals by smaller-scale motions. There is also some dynamical communication from the surface to the interior by downward *wave radiation*; for the most part this occurs as inertia-gravity waves that energize the interior wave field but do not greatly influence the currents.

There is, of course, reverse communication from the interior to the surface layer. Upwelled

waters carry heat, fresh water, and other materials, and the surface circulation has a substantial geostrophic component in addition to the Ekman currents. Lateral mixing by mesoscale eddies (Chap. 1; Sec. 8), generated by instabilities of the interior circulation, is also often important, although its effects can be secondary when the surface fields have quite large spatial scales and rather rapid time scales due to the air-sea coupling. On longer time scales the oceanic circulation is essential for Earth's climate (*e.g.,* Fig. 4). (See Chap. 10.)

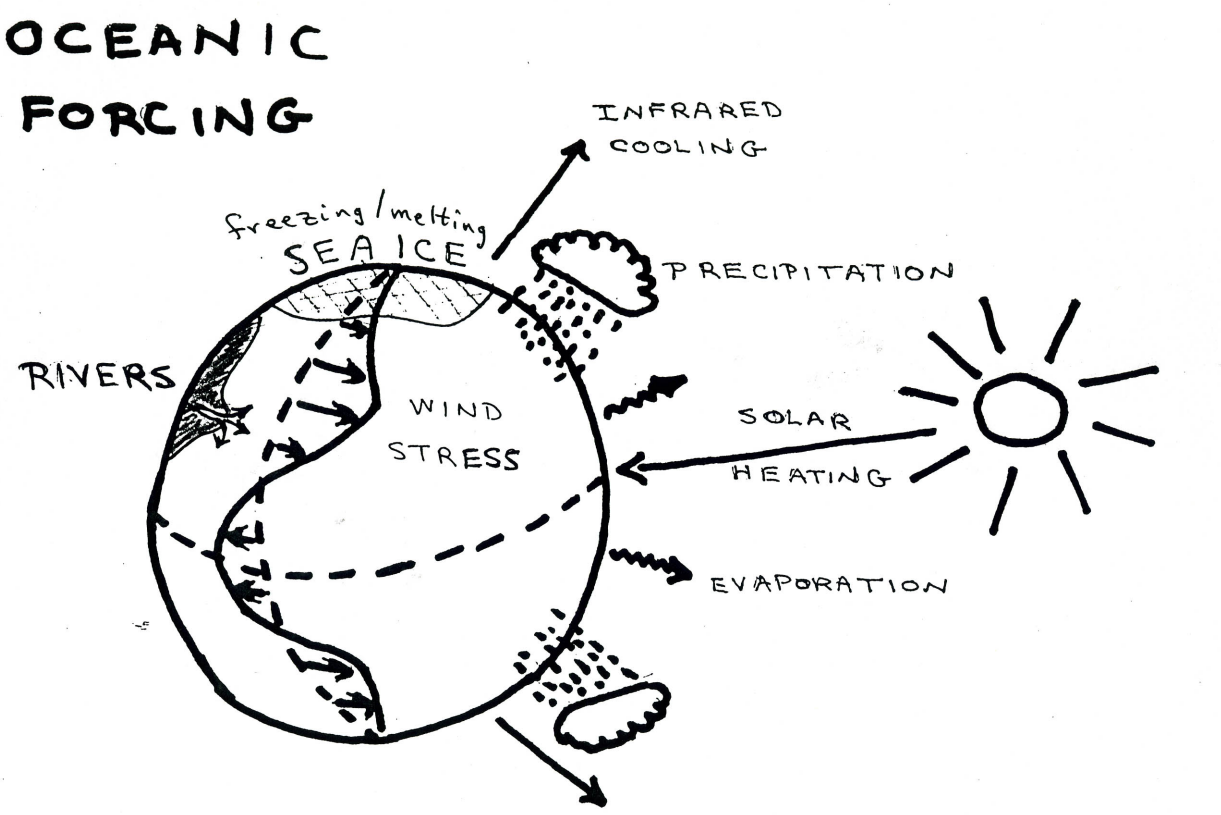


Figure 1: Cartoon of primary momentum, heat, and water forcings of the oceanic circulation.

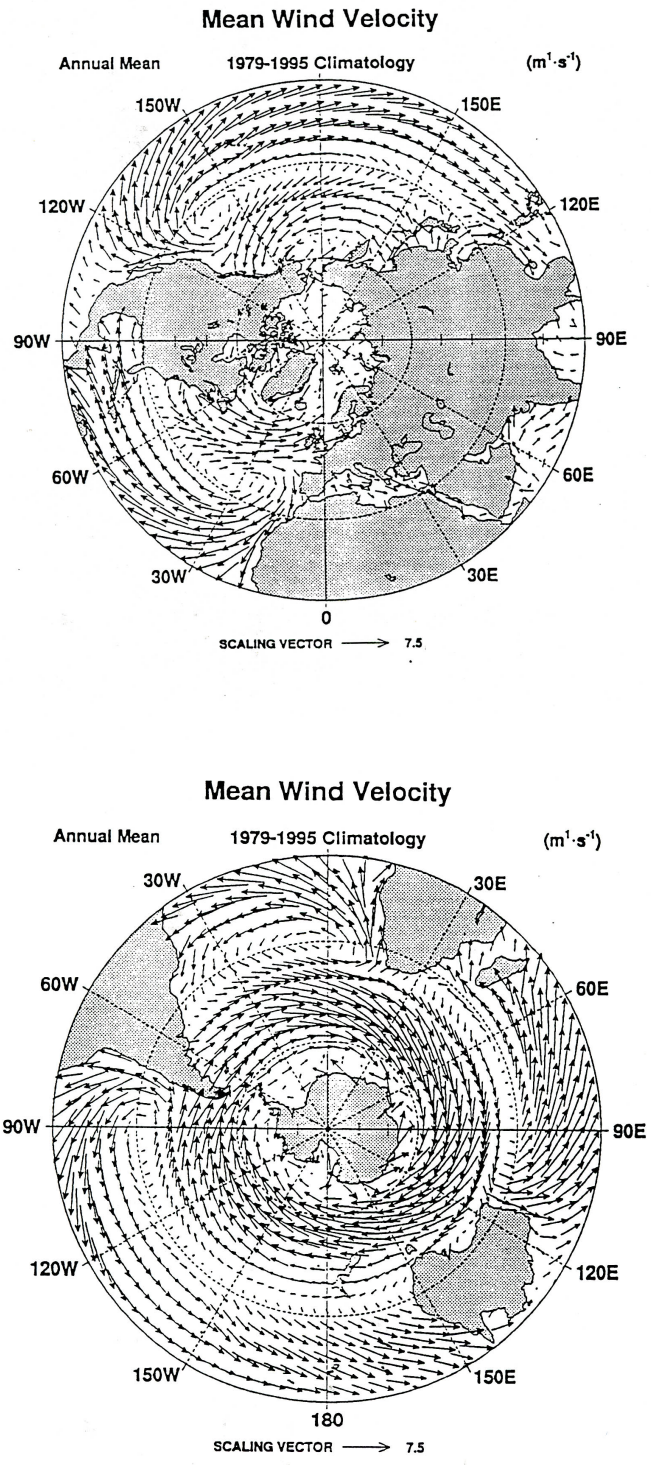


Figure 2: Annual-mean surface wind from the NCAR-NCEP reanalysis (Kalnay and co authors, 1996).

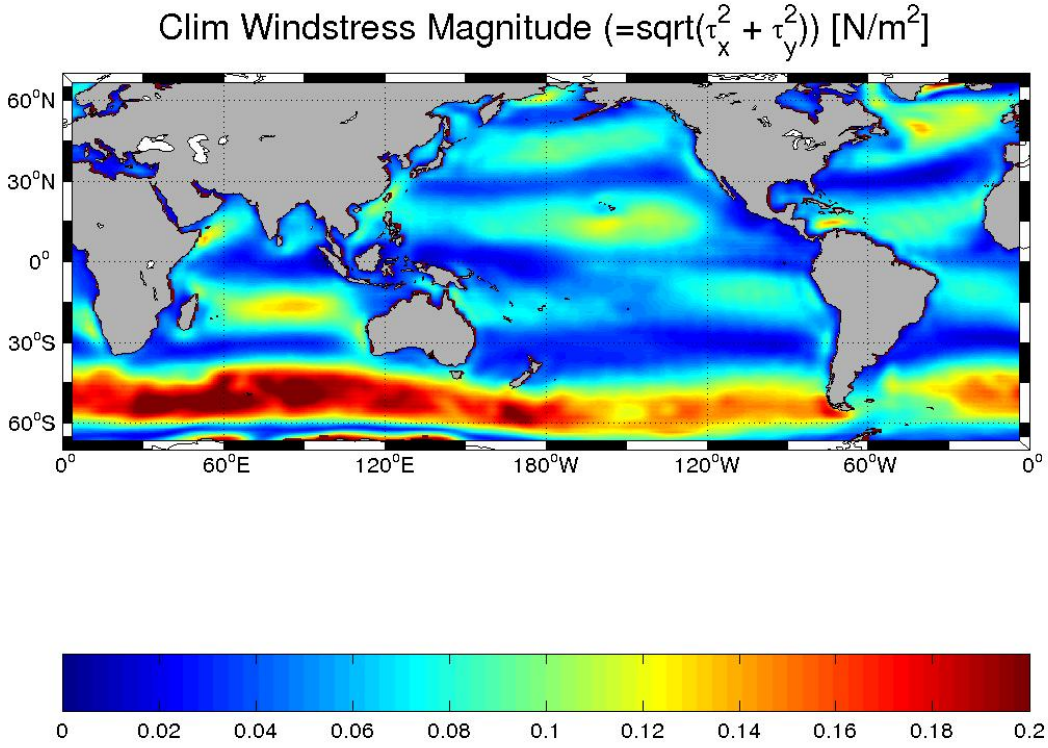


Figure 3: Annual-mean surface stress over the global ocean (Large and Yeager, 2004).

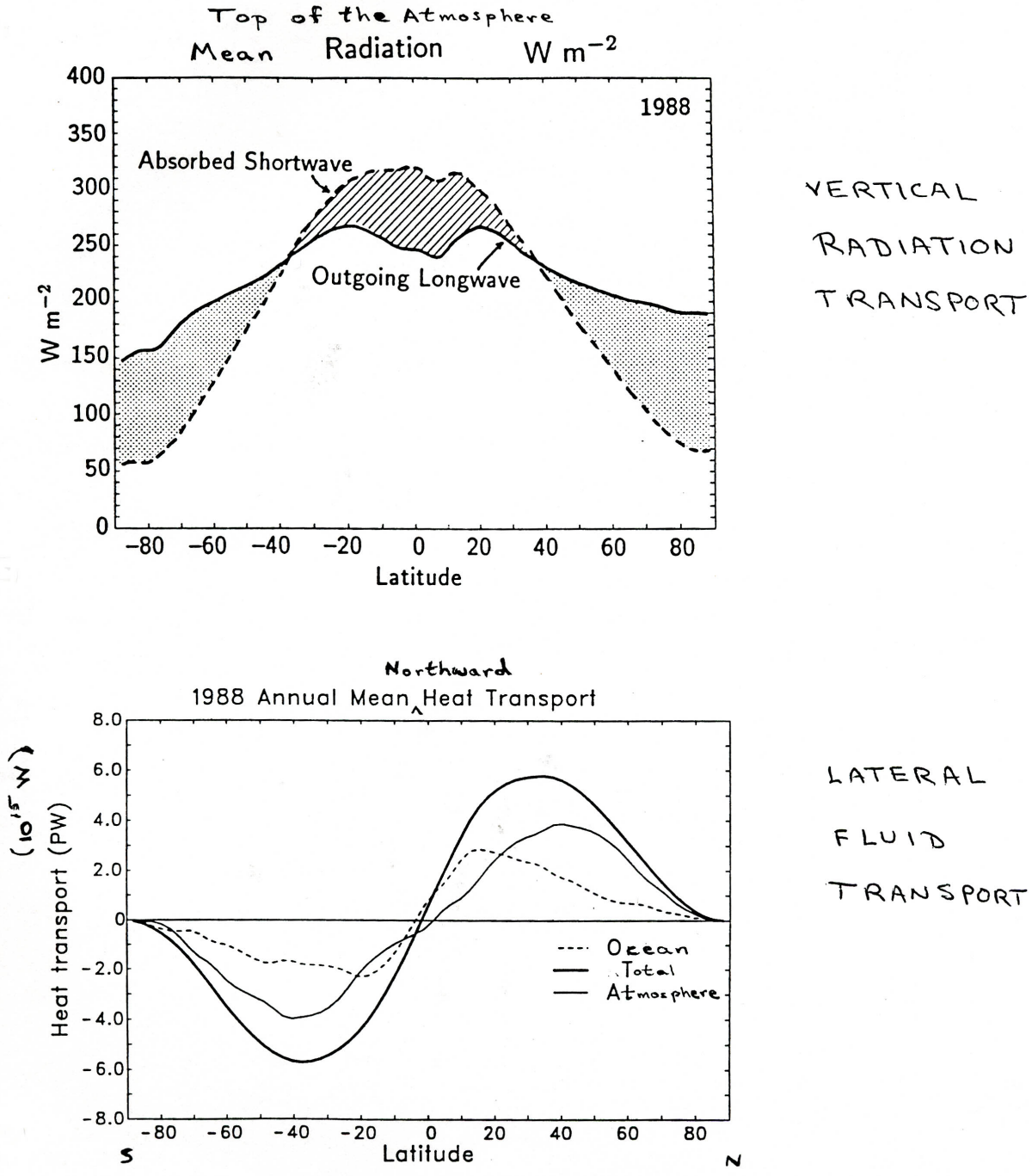


Figure 4: Annual- and zonal-mean meridional heat balance: (a) vertical energy flux at the top of the atmosphere, and (b) meridional flux, and partitioned into the oceanic and atmospheric parts (Trenberth and Solomon, 1994).

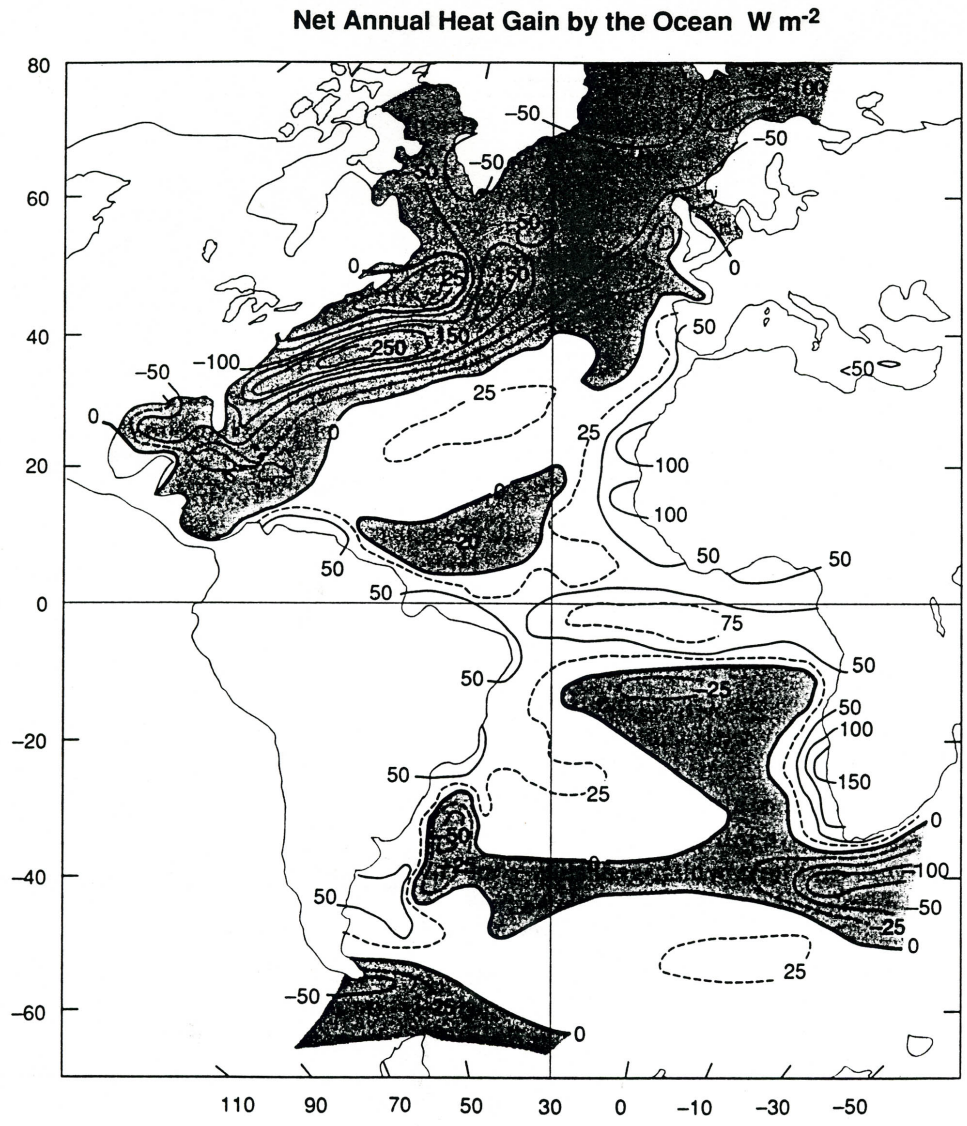


Figure 5: Annual-mean surface heat flux into the Atlantic Ocean (Niiler, 1992).

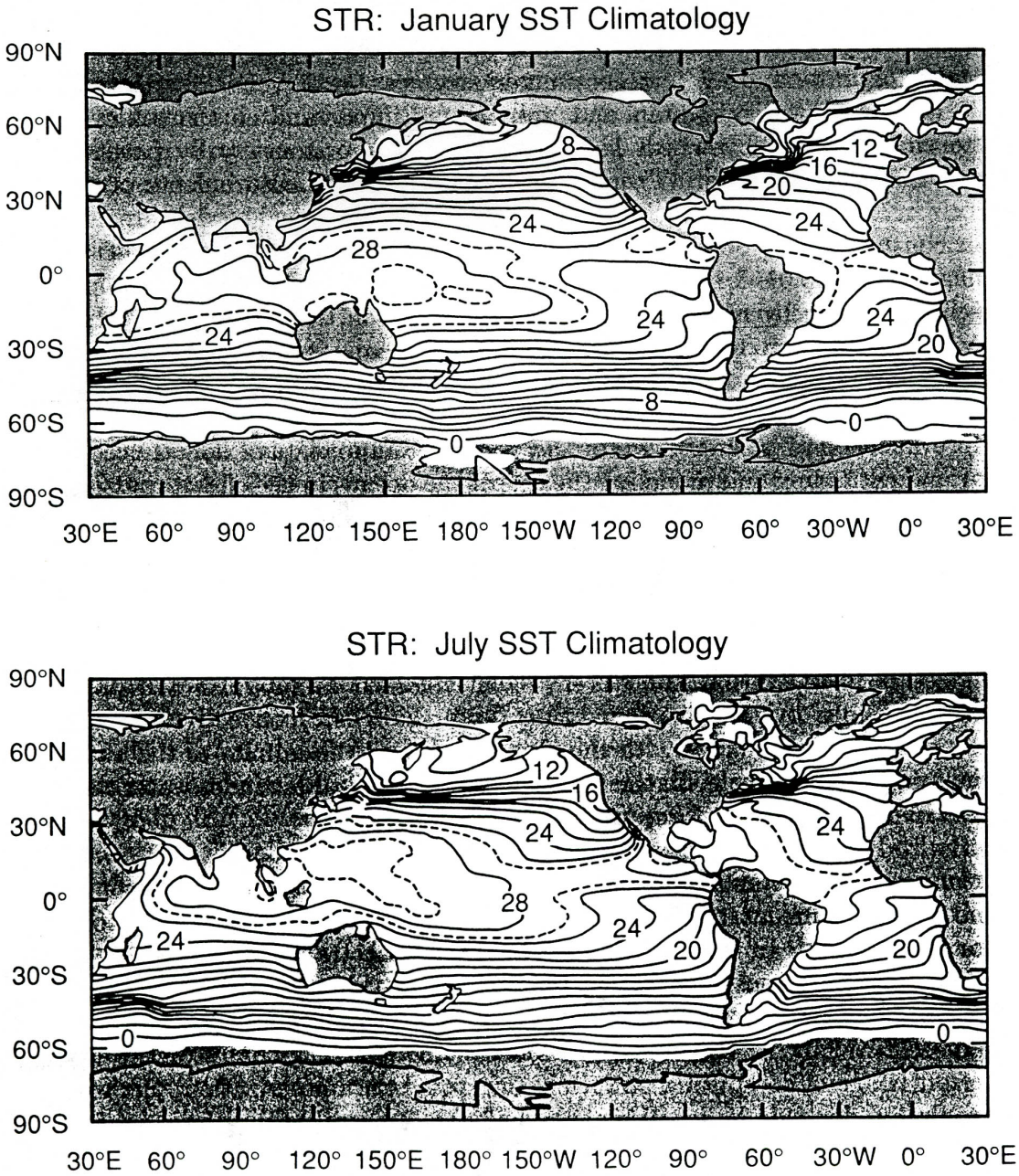


Monthly mean SSTs for January and July. Shaded areas indicate sea ice. The contour interval is 2°C except for dashed contours of 27 and 29°C. From Shea et al. (1990).

Figure 6: Mean summer and winter fields of sea surface temperature, SST (Niiler, 1992).

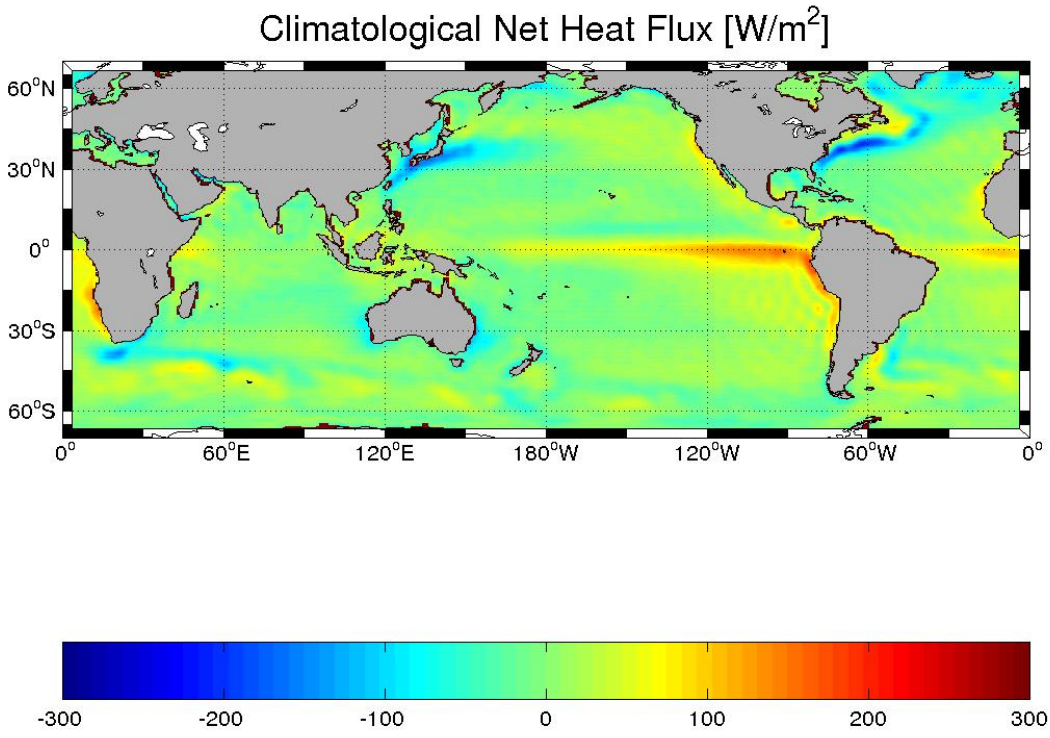


Figure 7: Annual-mean surface heat flux over the global ocean (Large and Yeager, 2004). This includes abosbed solar radiaion, absorbed and emitted infrared radiation, turbulent sensible and latent heat fluxes, and heats of freezing (warming sea water) and melting (cooling sea water) of sea ice.

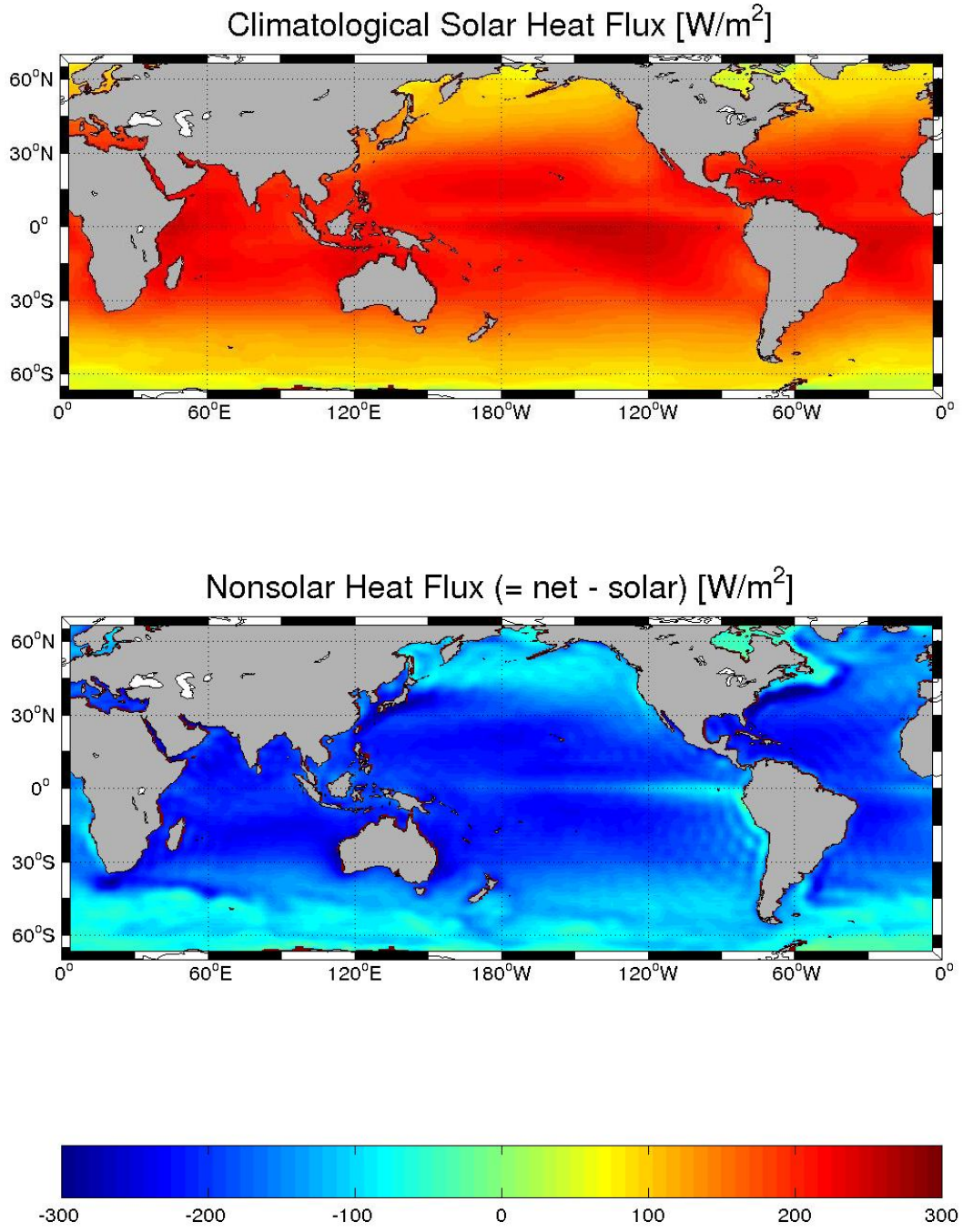


Figure 8: Annual-mean surface heat flux over the global ocean (Large and Yeager, 2004), decomposed into solar heating and the non-solar residual.

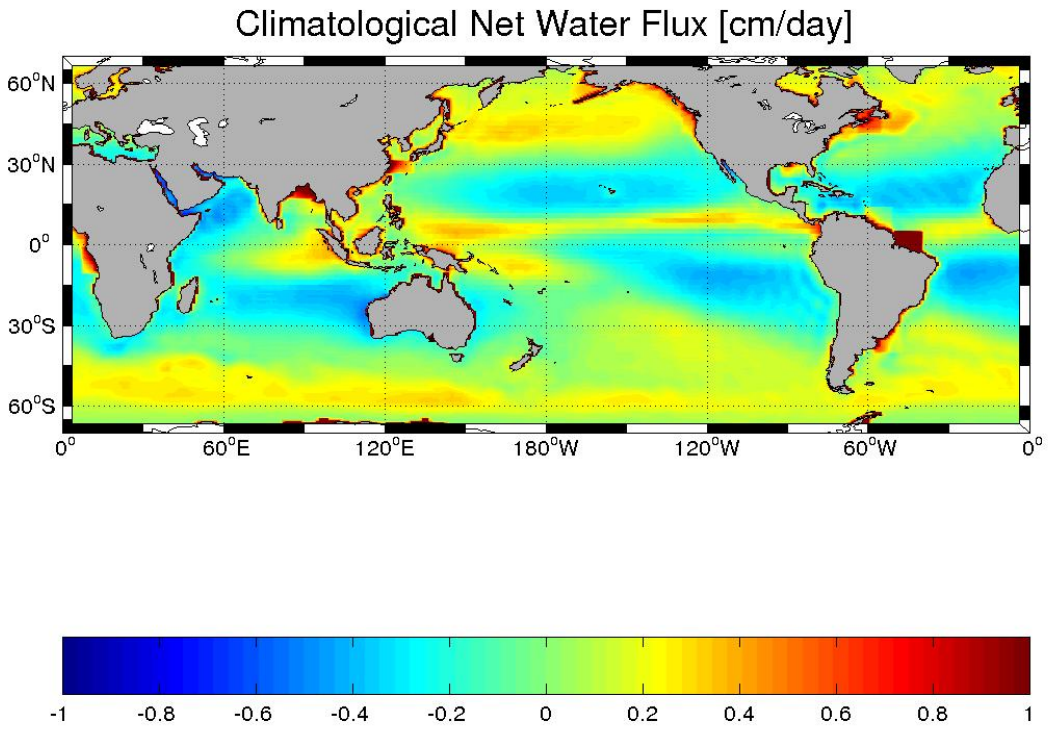


Figure 9: Annual-mean surface water flux over the global ocean (Large and Yeager, 2004). This includes precipitation, evaporation, riverine inflow, and the water exchanges by freezing (extrusion of salt into the sea water) and melting (supply or relatively fresh water) by sea ice.

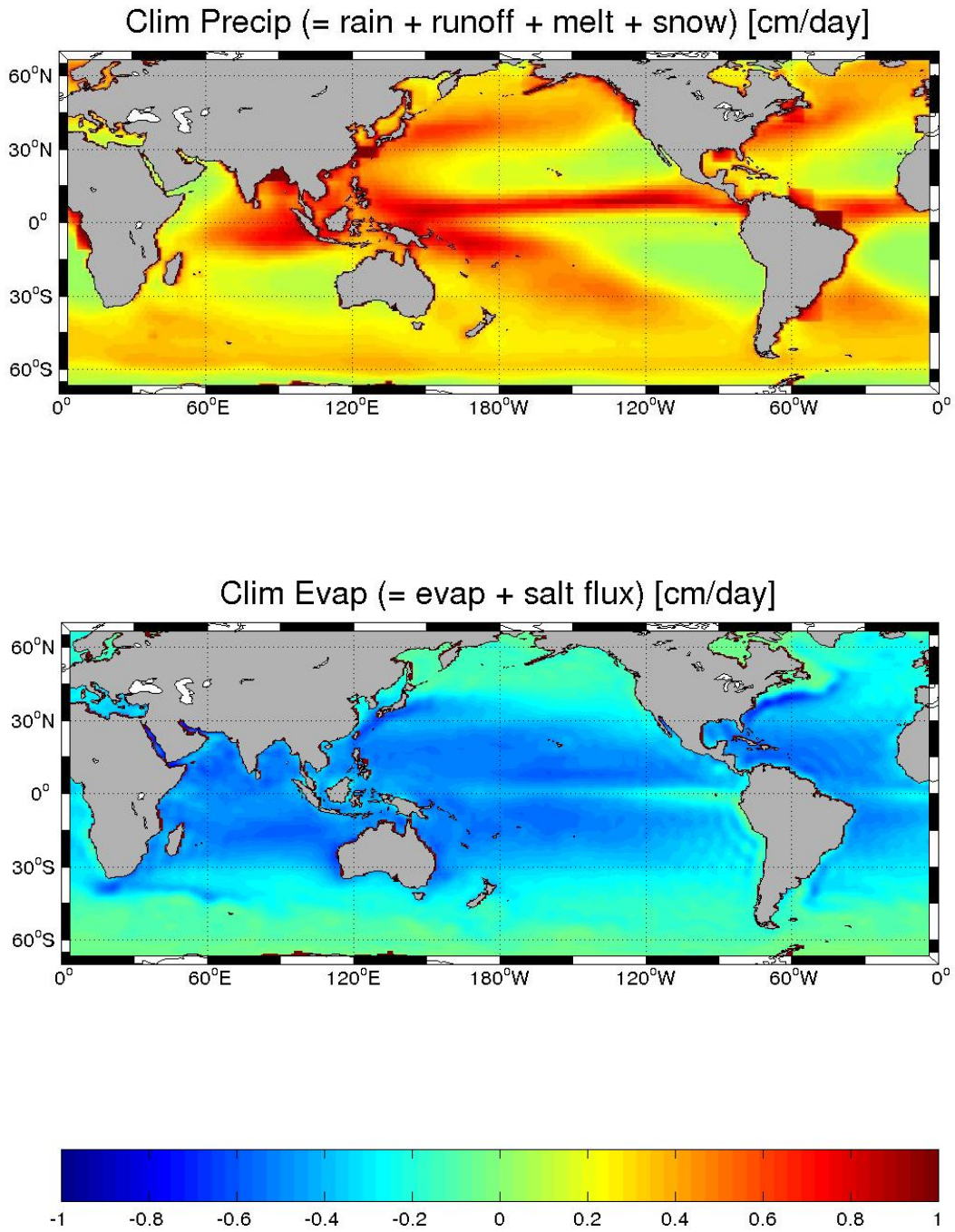


Figure 10: Annual-mean surface water flux over the global ocean (Large and Yeager, 2004), decomposed into the influx and outflux contributions.

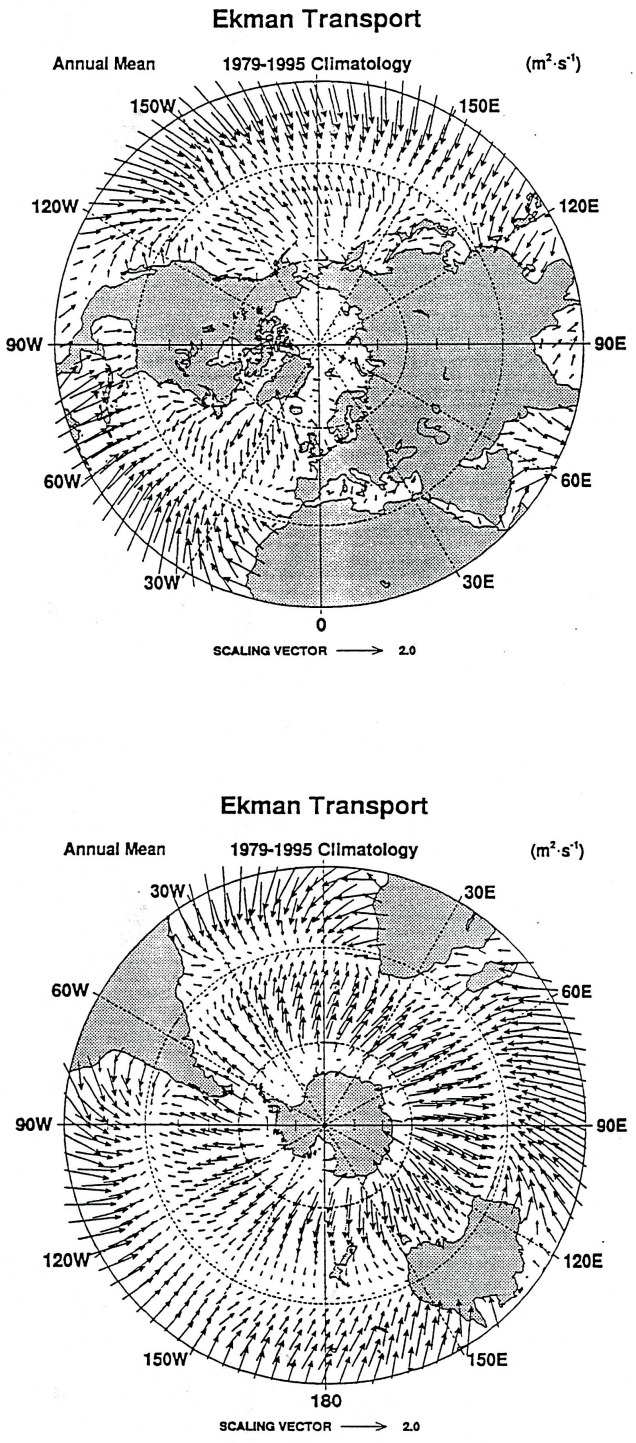


Figure 11: Annual-mean Ekman transport, $\mathbf{T}^t_{ek}$ [m$^2$s$^{-1}$] (McWilliams and Restrepo, 1999), based on the winds from the NCAR-NCEP reanalysis (Kalnay and co authors, 1996).

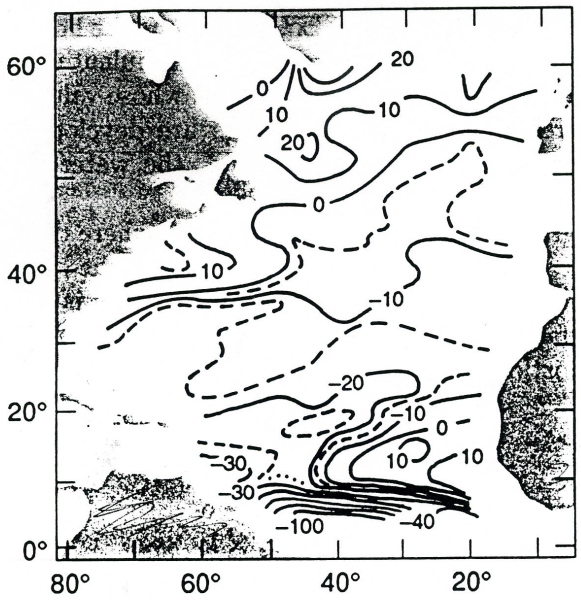


Annual mean North Atlantic vertical velocity at the base of the Ekman layer. Positive is upward and the units are in $10^{-8}$ cm $s^{-1}$. Note that off South America the contours between $-60$ and $-100$ are left out because of crowding (Leetmaa and Bunker, 1978).

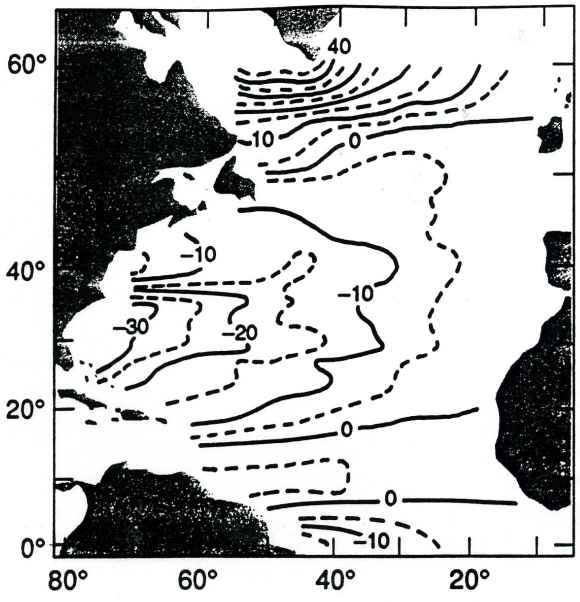


Ekman pumping & Sverdrup transport (Niiler, 1992).

Contours of the annual mean North Atlantic Sverdrup volume transport. Units are $10^6$ m $s^{-2}$ (Leetmaa and Bunker, 1978).

Figure 12: Annual-mean Ekman pumping, $w^t$, in the North Atlantic and the associated Sverdrup transport streamfunction, $Psi$ (Leetmaa and Bunker, 1978).

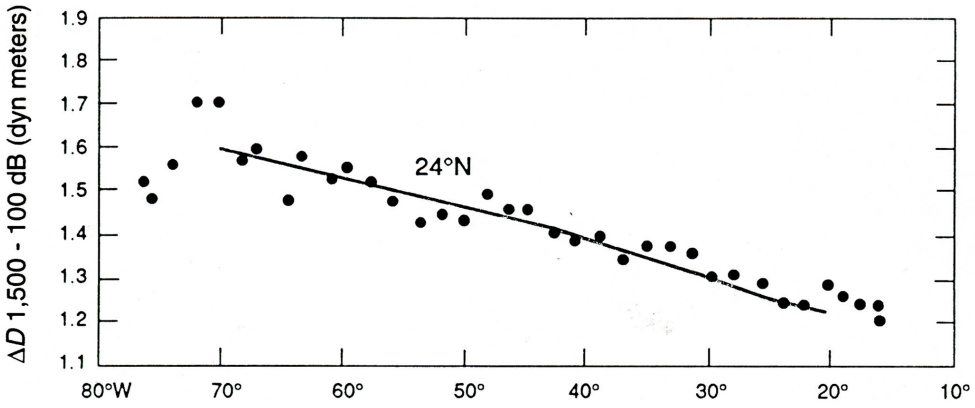


Dynamic height ($p/\rho_o$) (where $H = 1{,}500$ m) and the base of the Ekman layer is at 100 m, plotted for individual hydrographic stations vs. longitude along 24°N in the Atlantic. The light line displays the dynamic height computed from the curl of the wind stress forcing of the geostrophic transport per unit distance (after Leetmaa et al., 1977).

$$\beta \int_{-H}^{100\,m} dz\, v = f \hat{z} \cdot \nabla \times \left( \frac{\tau}{f} \right)$$

Figure 13: Demonstration of planetary vorticity balance and Ekman pumping in the Subtropical North Atlantic (Niiler, 1992).

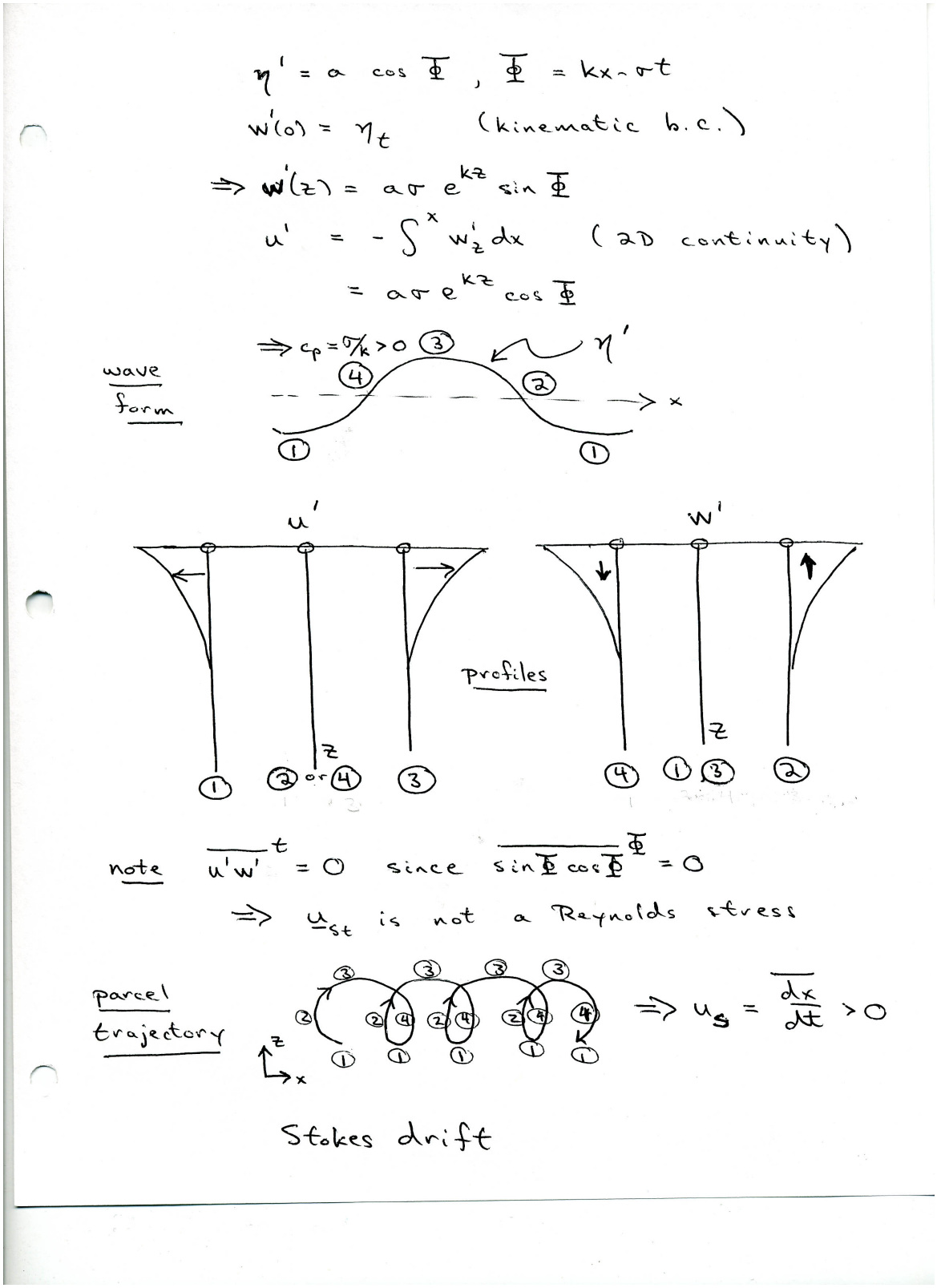


Figure 14: Cartoon of surface gravity wave motion and Stokes drift.

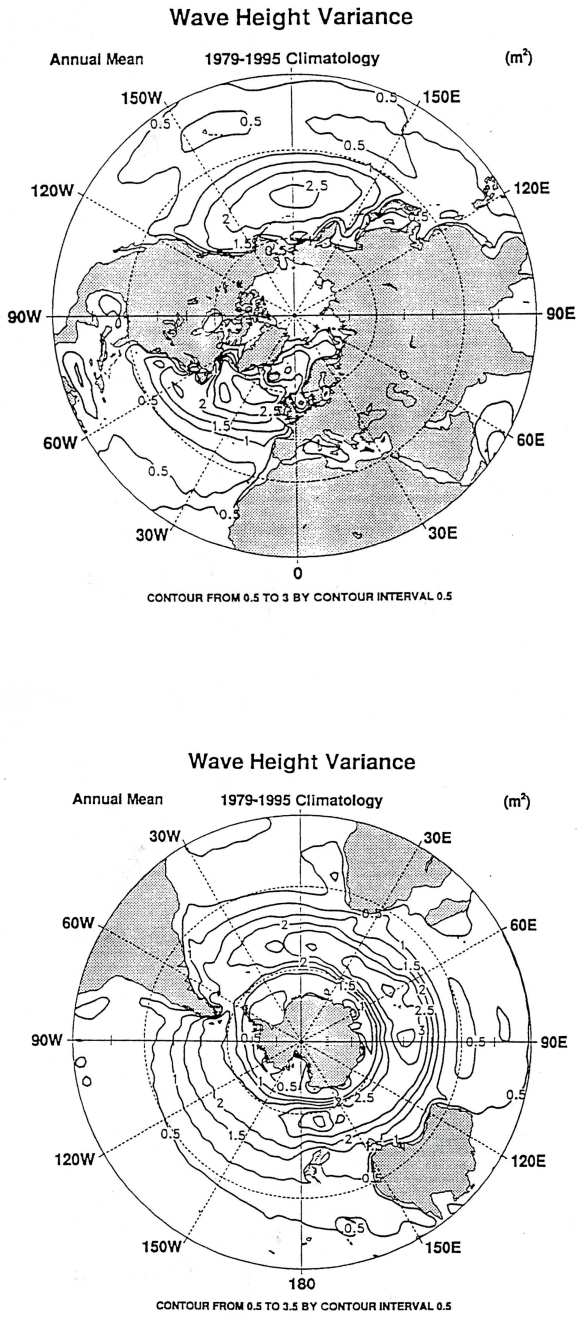


Figure 15: Annual-mean sea-level variance due to surface gravity waves, $overline\eta^2$ [m$^2$] (McWilliams and Restrepo, 1999), based on the winds from the NCAR-NCEP reanalysis (Kalnay and co authors, 1996) and the assumption of wind-wave equilibrium.

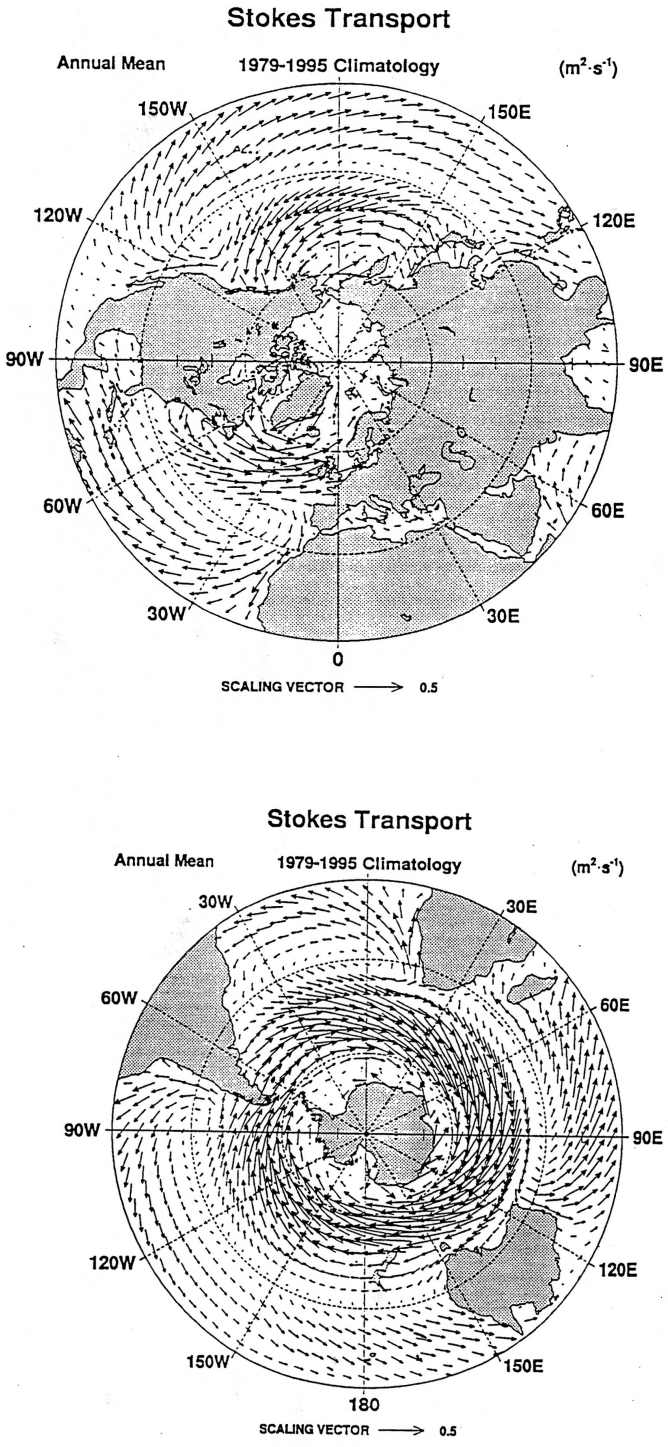


Figure 16: Annual-mean Stokes transport, $\mathbf{T}_{st}$ [$\mathrm{m^2 s^{-1}}$] (McWilliams and Restrepo, 1999), based on the winds from the NCAR-NCEP reanalysis (Kalnay and co authors, 1996) and the assumption of wind-wave equilibrium.

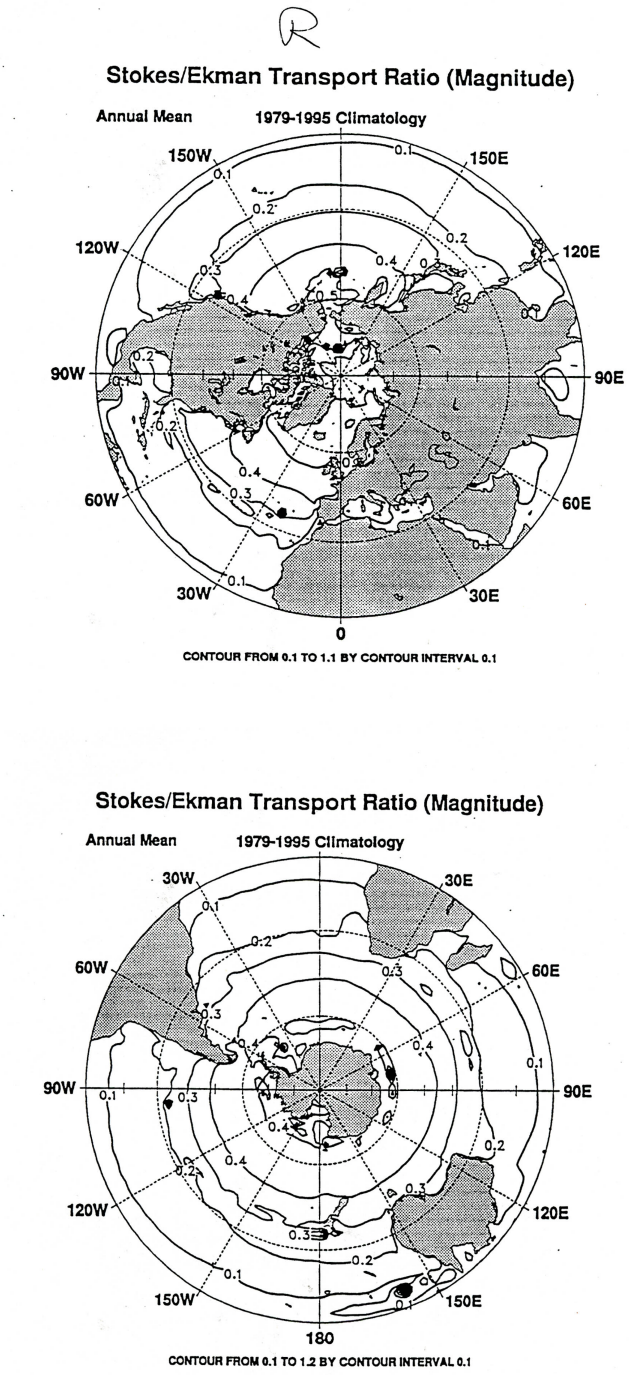


Figure 17: Ratio of annual-mean Stokes and Ekman transports (McWilliams and Restrepo, 1999).

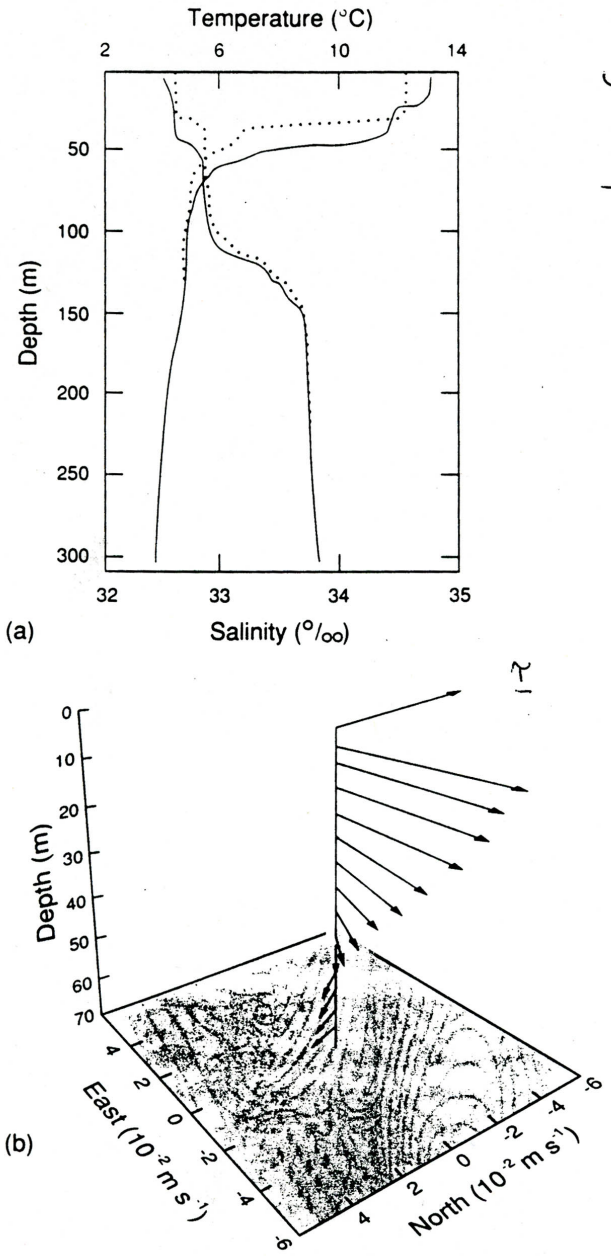


(a) Vertical distribution of temperature and salinity at 50°N., 145°W. in early September, 1977. The solid lines are before a storm and the dotted lines are after a storm, which depict the vertical mixing above the seasonal thermocline. The main thermocline, or pycnocline in this area is between 110 m and 160 m depth. (b) Time-averaged velocity for a 25 day summer period at an open ocean site southwest of Bermuda. Current meter measured velocity is referenced to 70 m. The topmost dashed vector is the time-averaged wind stress (Price et al., 1986).

Figure 18: Summertime upper-ocean profiles of $\mathbf{u}_h$, $T$, and $S$ in the North Pacific and North Atlantic (Niiler, 1992).

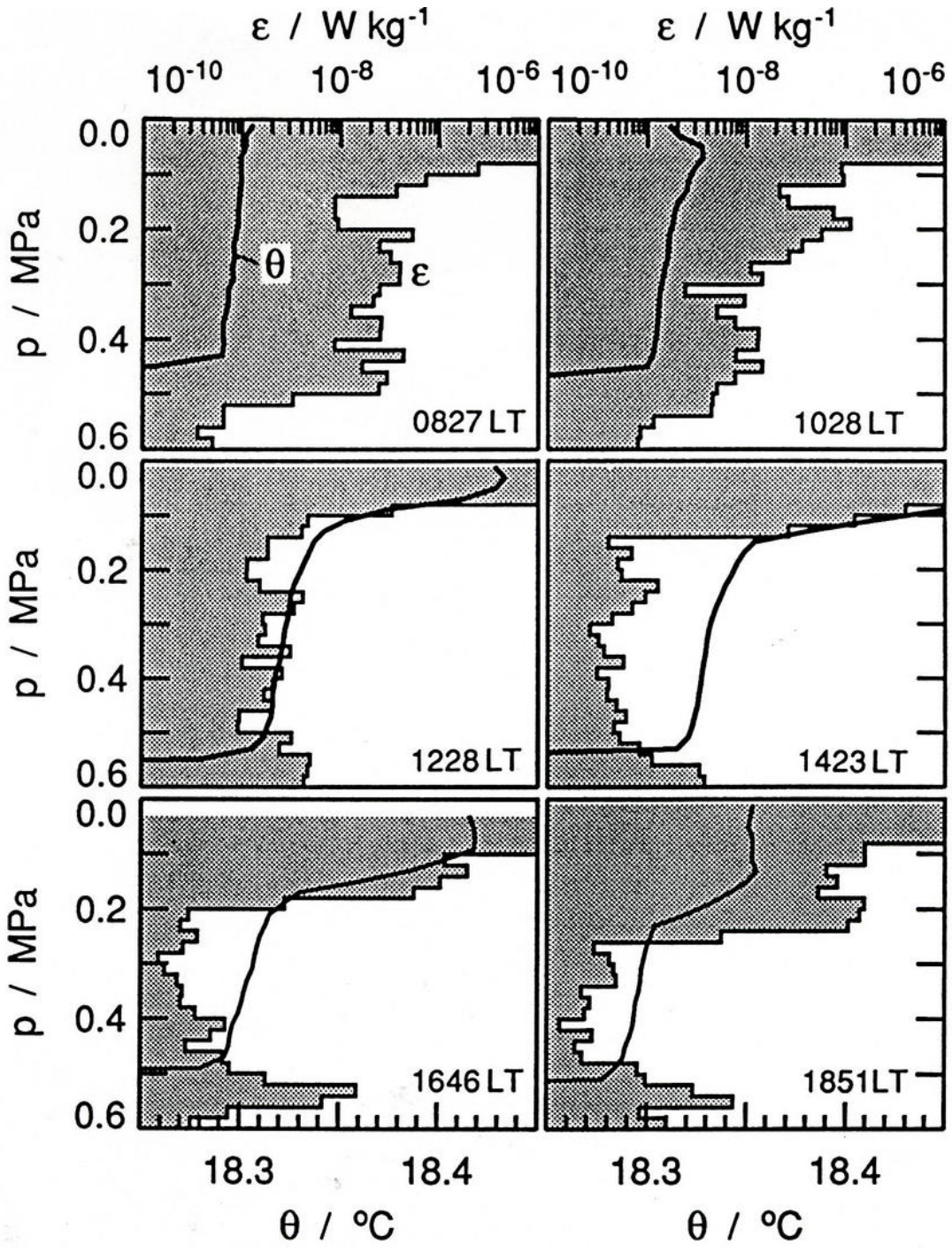


Figure 19: Profiles of hour-averages of dissipation rate $\epsilon$ (shaded) and potential temperature $\theta$ through part of a diurnal cycle (Brainerd and Gregg, 1993). LT denotes local time, and the depth unit is approximately equivalent to 100 m.

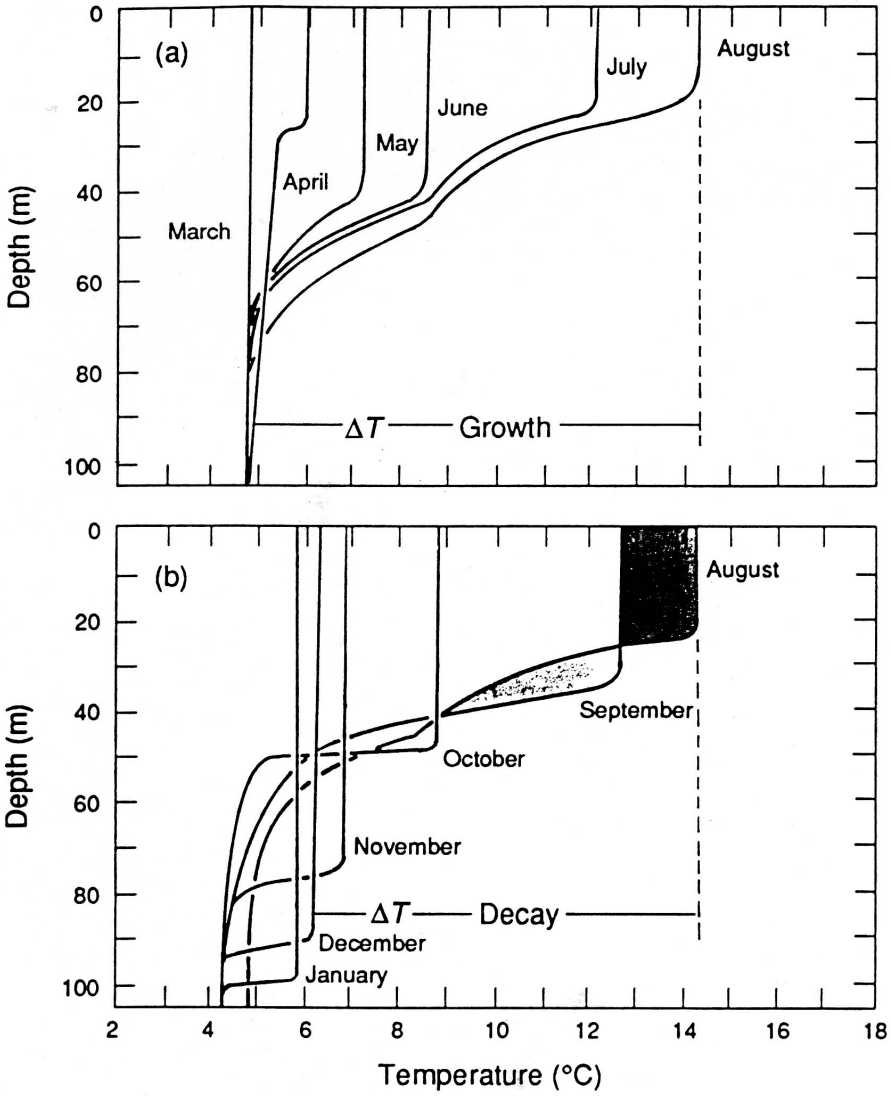


The development of the seasonal thermocline in the eastern North Pacific in the vicinity of 50°N, 145°W. The warming of SST from March to August is due to progressively warmer layers being formed during net heating of the ocean. The cooling from August to September is due to vertical mixing, because equal volumes of cold and warm water are exchanged vertically. Cooling of this area sets in from October onward (Tully and Giovando, 1963).

Figure 20: Annual cycle of the surface mixed layer in the Eastern North Pacific (Niiler, 1992).

# References


Brainerd, K. and M. Gregg, 1993: Diurnal restratification and turbulence in the oceanic surface mixed layer 1. Observations. *J. Geophys. Res.*, **98**, 22645–22656.

Craik, A. and S. Leibovich, 1976: A rational model for Langmuir circulations. *J. Fluid Mech.*, **73**, 401–426.

Kalnay, E. and co authors, 1996: The ncep/ncar 40-year reanalysis project. *Bull. Am. Meteorol. Soc.*, **77**, 437–471.

Large, W., 1998: Modeling and parameterizing ocean planetary boundary layers. *Ocean Modeling and Parameterization*, E. C. . J. Verron, ed., Kluwer, 81–120.

Large, W., J. McWilliams, and S. Doney, 1994: Oceanic vertical mixing: A review and a model with a non-local K-profile boundary layer parameterization. *Rev. Geophys.*, **32**, 363–403.

Large, W. and S. Yeager, 2004: Diurnal to decadal global forcing for ocean and sea-ice models: the data sets and flux climatologies. *NCAR Technical Note*, **TN-460+**.

Leetmaa, A. and A. Bunker, 1978: Updated charts of the mean annual wind stress, convergences in Ekman layers, and Sverdrup transports in the North Atlantic. *J. Mar. Res.*, **36**, 311–322.

McWilliams, J. and J. Restrepo, 1999: The wave-driven ocean circulation. *J. Phys. Ocean.*, **29**, 2523–2540.

McWilliams, J., J. Restrepo, and E. Lane, 2004: An asymptotic theory for the interaction of waves and currents in coastal waters. *J. Fluid Mech.*, **511**, 135–178.

McWilliams, J., P. Sullivan, and C. Moeng, 1997: Langmuir turbulence in the ocean. *J. Fluid Mech.*, **334**, 1–30.

Munk, W., 1950: On the wind-driven ocean circulation. *Journal of Meteorology*, **7**, 79–93.

Niiler, P., 1992: The ocean circulation. *Climate System Modeling*, K. Trenberth, ed., Cambridge University Press, 117–148.

Pierson, W. and L. Moskowitz, 1964: A proposed spectral form for fully developed wind seas based on the similarity theory of s. a. kitaigorodskii. *J. Geophys. Res.*, **69**, 5181–5190.

Robinson, A., 1963: *Wind-driven Ocean Circulation: A Collection of Theoretical Studies*. Blaisdel, 161 pp.

Stommel, H., 1948: The westward intensification of wind-driven ocean currents. *Trans. Amer. Geophys. Union*, **29**, 202–206.

Trenberth, K. and A. Solomon, 1994: The global heat balance: Heat transports in the atmosphere and ocean. *Clim. Dyn.*, **10**, 107–134.